

Amplified up-conversion of electromagnetic waves using time-varying metasurfaces

Fedor Kovalev,^{1,*} Stanislav Maslovski,² Abdelghafour Abraray,² and Ilya Shadrivov¹

¹ ARC Centre of Excellence for Transformative Meta-Optical Systems (TMOS), Research School of Physics, The Australian National University, Canberra ACT 2601, Australia

² Instituto de Telecomunicações and Department of Electronics, Telecommunications and Informatics, University of Aveiro, Aveiro, 3810 – 193, Portugal

ABSTRACT. Time-varying metamaterials and photonic time crystals offer a powerful route to wave amplification through temporal modulation of material parameters. Here, we experimentally demonstrate amplified up-conversion of free-space electromagnetic waves in the microwave regime, with conversion efficiency exceeding the limits imposed by the Manley–Rowe relations as a result of a cascaded amplification process. Using a time-varying metasurface composed of an array of varactor-loaded coupled split-ring resonators, we investigate parametric amplification, frequency up-conversion and wave generation. Direct measurements in both non-degenerate and degenerate regimes show that the Manley–Rowe limits can be surpassed near integer multiples of the incident wave frequency when the pump frequency is approximately twice that of the incident wave. These results establish time-varying metasurfaces as an efficient platform for amplification, generation, and frequency conversion of electromagnetic waves in the microwave and terahertz bands, with potential extension to optical frequencies via ultrafast modulation techniques.

I. INTRODUCTION

In time-varying or parametric metasurfaces, the physical parameters are modulated in time by an external energy source [1,2]. Time-varying media were first investigated more than fifty years ago [3–5] and have recently emerged as a highly promising area in metamaterial research [6,7], driven by the development of materials capable of ultrafast parameter modulation. The time dimension takes metasurface concept to a whole new level [6,8]. Time-varying metasurfaces (TVM) with physical parameters modulated in time go beyond the limits of passive electromagnetic media [9]. Such metasurfaces enable a range of non-trivial physical effects, including nonreciprocity [10–12], in which electromagnetic waves are transmitted differently when propagating in opposite directions. Recently, time-varying metasurfaces have enabled the realisation of photonic time crystals [13], a form of matter structured in time and analogous to conventional crystals structured in space, providing a new platform for the amplification of electromagnetic waves [14]. TVMs have also facilitated the demonstration of a temporal analogue of the Young’s double-slit diffraction experiment [15]. Modulation of metasurface parameters over time gives rise to generation of new frequency harmonics when electromagnetic waves interact with such media, enabling frequency conversion [1,16]. Moreover, temporal interfaces recently demonstrated such exotic

effects as time refraction and reflection [17–20], temporal counterparts of classical spatial physical processes.

Recent advances in TVMs have established them as a powerful platform for amplification, where temporal modulation and resonant enhancement allow electromagnetic waves to efficiently extract energy from the modulation process [21–26]. These results show that TVMs can not only convert and redistribute spectral content with high flexibility but also overcome the fundamental limitations of passive electromagnetic systems by providing controllable gain, paving the way for applications ranging from wireless communications to compact light sources. Amplification using TVMs have recently attracted significant attention owing to advances in ultrafast modulation techniques, which hold promise for its implementation at optical frequencies [19].

In this work, we experimentally demonstrate amplified up-conversion of *free-space electromagnetic waves* using TVMs. The proposed parametric meta-atoms achieve up-conversion gains exceeding 10 dB in the degenerate regime and 5 dB in the non-degenerate regime. The experimental results further confirm that, in certain cases, the up-conversion efficiency is not limited by the Manley–Rowe relations [27], owing to a cascaded amplification mechanism [28]. Notably, when the pump power approaches the self-excitation threshold, the radiated power at the sum frequency, which is approximately three times higher than the signal frequency, exceeds the incident signal power by

more than a factor of three in both regimes. These findings open pathways toward applications in microwave and terahertz communications, including compact solutions for the generation, amplification, and frequency conversion of electromagnetic waves. The demonstrated concept can be extended to higher-frequency regimes through the implementation of ultrafast modulation and carefully engineered resonant responses.

II. MODELING RESULTS

Figure 1 shows the proposed TVM, whose meta-atoms consist of dual split-ring resonators loaded with varactor diodes. The varactor capacitances are modulated by an external pump source through a biasing network at the frequency f_p . When an incident “signal” wave at f_s interacts with the TVM, combination frequencies are generated, including the sum-frequency component $f_{sum1} = f_s + f_p$.

The meta-atom consists of two connected split-ring resonators with the varactor diode (MGV100-20) embedded in the gap as illustrated in Figure 2(a). We first simulate the metasurface characteristics for two varactor diode capacitance values under the corresponding dc reverse voltage in CST Studio. See the meta-atom design and simulation details in the Supplemental Material.

Figure 2(b) shows the reflection characteristics of the metasurface for two constant applied dc voltages (U_0). Two narrow resonances at f_s and f_{sum1} shift with variations in the applied voltage. The meta-atom geometry was optimised so that these resonances satisfy the approximate relation $f_{sum1} \approx 3f_s$. A broad resonance is also observed at $f_{sum2} \approx 5f_s$ in the spectrum, and its central frequency shifts with the applied dc bias voltage.

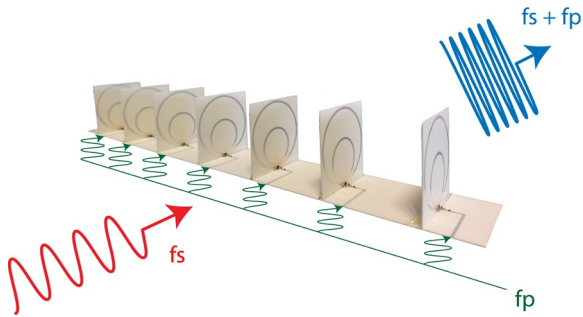


FIG 1. Schematic representation of amplified up-conversion by a TVM. An electromagnetic wave at f_s is incident on the TVM, whose meta-atoms are modulated by a pump source at f_p , resulting in amplification and frequency conversion to the sum-frequency $f_s + f_p$.

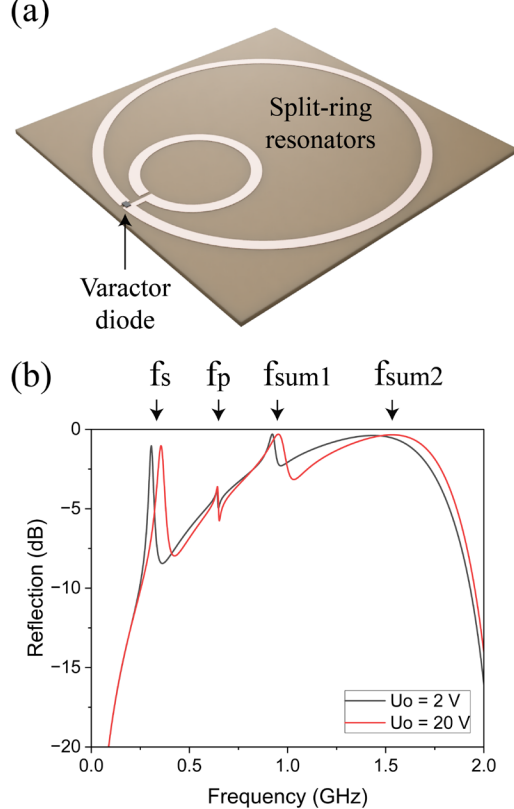


FIG 2. (a) Time-varying meta-atom consisting of two connected split-ring resonators with the embedded varactor diode. (b) Reflection characteristics of the metasurface for two applied dc voltage values (U_0).

The peak at f_p does not originate from the meta-atom geometry itself, it appears in reflection due to the passband filter connected to the SRRs for protecting the ac pump source from the dc bias and currents at the signal and sum frequencies. We specifically choose $f_p \approx 2f_s$ and tune the resonances to the multiples of f_s for utilizing the cascaded parametric amplification process allowing to overcome the limit imposed by Manley-Rowe relations [28].

The maximum possible conversion efficiency for the sum-frequency is determined by the Manley-Rowe relations:

$$K_P = \frac{P_{sum}}{P_s} = \frac{f_{sum}}{f_s}, \quad (1)$$

where P_{sum} is the generated power at f_{sum} , P_s is the power of the incident wave and P_p is the power of the pump source. In Eq. (1), it is assumed that the power of the incident wave and the pump source is fully utilized in the mixing process.

Next, we discuss the results of the TVM modeling obtained in CST Studio and show that it is possible to overcome this limit when $f_{sum} \approx 3f_s$. See the simulation details in the Supplemental Material.

*Contact author: fedor.kovalev@anu.edu.au

We modulate the varactor diodes integrated into the gaps of the dual split-ring resonators with the following pump voltage applied through microstrip lines and appropriate filtering circuits:

$$u_p(t) = U_0 + U_p \cos(\omega_p t + \varphi_p), \quad (2)$$

where U_0 is the constant dc bias voltage, U_p is the pump amplitude, $\omega_p = 2\pi f_p$ is the pump frequency, φ_p is the pump phase.

Figure 3(a) shows the dependence of the total radiated power at $f_s = 320$ MHz, $f_{sum1} = 960$ MHz and $f_{sum2} = 1600$ MHz on the pump amplitude U_p at $f_p = 640$ MHz, for $U_0 = 10$ V under the condition of phase locking in the degenerate regime. The dashed horizontal line indicates the incident “signal” wave power at f_s , equal to $0.25 \mu\text{W}$. The shaded region marks the range where the varactor model becomes inaccurate according to the manufacturer ($U_p > 7.5$ V). Nevertheless, the selected varactor diodes operate in reverse bias from 0 to 22 V, with the latter value corresponding to breakdown. The results shown in Fig. 3 lie within this range.

Figure 3(a) shows that the total power radiated at f_s increases rapidly once the pump amplitude exceeds 7 V, while remaining nearly constant below this threshold. The radiated power at both sum-frequency components also rises sharply with increasing pump amplitude. Figure 3(a) further demonstrates that *the overall radiated power at f_{sum1} exceeds the input signal power*, indicating efficient up-conversion with gain. In particular, at a pump amplitude of $U_p = 9$ V, the overall radiated power at f_{sum1} is more than forty times larger than the incident power at f_s , corresponding to a gain of approximately 16 dB. Moreover, under the same conditions, the radiated power at f_{sum1} exceeds the amplified power radiated at f_s by more than a factor of four. According to the Manley–Rowe relations, the maximum achievable power gain at f_{sum1} with respect to the incident signal power is limited by the frequency ratio f_{sum1}/f_s and in this case is equal to three.

Figure 3(b) demonstrates that, in the non-degenerate regime, the overall radiated power at f_{sum1} exceeds the input power at f_s by more than an order of magnitude when the pump amplitude reaches 9 V and the pump frequency is set near the degenerate case ($f_p = 639.9$ MHz). However, when the pump amplitude remains within the range of validity of the varactor model (below 7.5 V), the radiated power at both sum frequencies is lower than the incident power at f_s . The amplification and up-conversion characteristics in the non-degenerate regime closely resemble those obtained in the degenerate case. In the non-degenerate regime, the efficiency is reduced due to the simultaneous generation of power at the idler frequencies f_i , f_{sum1i} and f_{sum2i} .

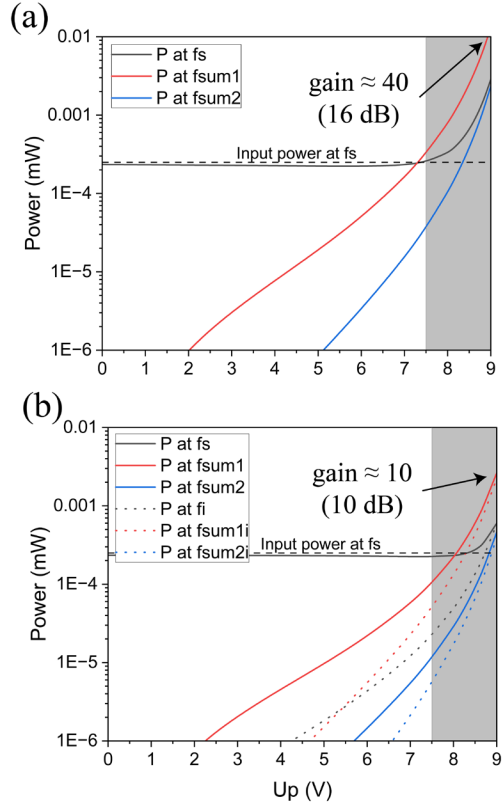


FIG 3. Calculated radiated power as a function of pump amplitude for $U_0 = 10$ V (logarithmic scale). (a) Degenerate regime under phase-locking conditions with $f_s = 320$ MHz, $f_p = 640$ MHz, $f_{sum1} = 960$ MHz and $f_{sum2} = 1600$ MHz; (b) Non-degenerate regime with $f_s = 320$ MHz, $f_i = 319.9$ MHz, $f_p = 639.9$ MHz, $f_{sum1} = 959.9$ MHz, $f_{sum1i} = 959.8$ MHz, $f_{sum2} = 1599.9$ MHz and $f_{sum2i} = 1599.8$ MHz. The input power level of the “signal” wave is indicated by the horizontal dashed line. The shaded region corresponds to $U_p > 7.5$ V, where the varactor model becomes inaccurate according to its datasheet.

III. EXPERIMENTAL RESULTS

Next, we describe the meta-atom design used in the experiments. Figure 4 presents the structure, which consists of two circuits fabricated on Rogers RO4350B substrates. The horizontal circuit board serves several functions: it supplies the pump power to the varactor diode, provides its dc bias and connects the split-ring resonators to the ground through a via. The back side of the substrate of the horizontal circuit board is copper-coated and functions as a ground plane. This arrangement provides the required isolation between the propagating electromagnetic wave and the pump circuit, ensuring that their

*Contact author: fedor.kovalev@anu.edu.au

influence on wave propagation is negligible. Each vertical board incorporates two connected copper split-ring resonators with an embedded MGV100-20 varactor diode and a blocking capacitor of 1 nF to protect the dc source connection to ground via the outer ring. The ac microstrip line provides pumping of the varactor diode through a passband filter consisting of inductor of 130 nH and capacitor of 0.1 pF, driven by a 50Ω microwave generator. The dc microstrip line includes an inductor (RF choke) of 500 nH to block ac currents from reaching the dc source. See the details of the meta-atom design and geometry in the Supplemental Material.

We used a transverse electromagnetic (TEM) cell to emulate the response of the meta-atoms under plane-wave incidence. TEM cells offer a controlled environment for generating plane waves in a compact setting and detecting radiation from meta-atoms. Functioning as waveguides, they convert electrical signals into nearly homogeneous electromagnetic fields with a transverse mode distribution, closely resembling free-space conditions in modeling. See the details of the TEM cell geometry, modeling of time-varying meta-atoms in the TEM cell and measurements involved in the experiments in the Supplemental Material.

Figure 5(a) shows a photograph of the fabricated meta-atoms placed inside the TEM cell, along with biasing cables for connecting to a dc source and coaxial connectors for applying the ac pump modulation at f_p . Figure 5(b) presents the reflection characteristics of the meta-atoms within the TEM cell obtained from both simulations and experiments. Two resonances are observed at f_s and f_{sum1} (around 320 and 960 MHz, respectively, indicated by vertical lines for clarity).

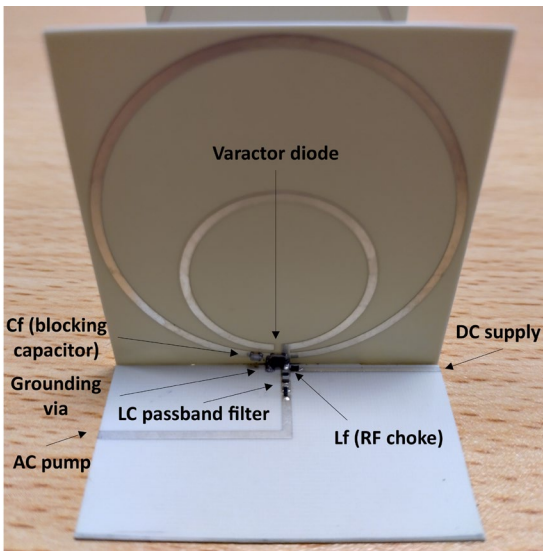


FIG 4. (a) Photograph of the fabricated meta-atom with soldered lumped elements.

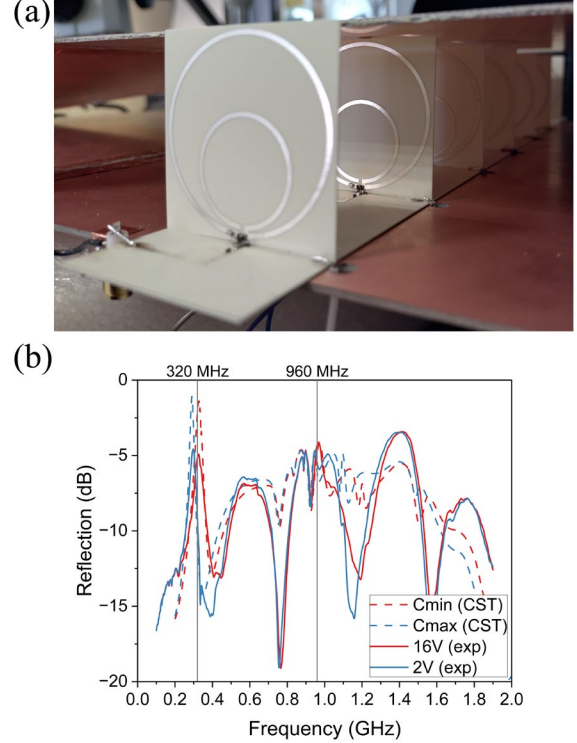


FIG 5. (a) Photograph of the fabricated meta-atoms inside the designed TEM cell. (b) Reflection characteristics of the meta-atoms in the TEM cell: simulations vs. experiments.

The resonances shift with changes in the capacitance of the varactor diodes in modeling and with the applied dc voltage in the experiments. Both simulation and experimental results show that the reflection level at f_{sum1} is relatively low, primarily due to additional radiation and ohmic losses in the TEM cell at this frequency. The resonance at f_s exhibits a reflection level that is more than 3 dB lower in experiments compared to simulations. This discrepancy is most likely caused by imperfect positioning of the meta-atoms within the TEM cell and fabrication imperfections.

Significant up-conversion efficiency was experimentally achieved at a reduced dc bias voltage of $U_0 = 4$ V with pump power levels of up to 37 dBm at the output of the power amplifier, prior to splitting among the seven meta-atoms. These values of the dc bias voltage in our experiments have enabled additional investigation of the self-excitation threshold and parametric generation.

Figure 6 shows the dependence of the overall radiated power at $f_s = 316$ MHz, $f_{sum1} = 948$ MHz and $f_{sum2} = 1580$ MHz on the pump power at $f_p = 632$ MHz (at the output of the power amplifier) for $U_0 = 4$ V under phase-locking in the degenerate regime (logarithmic scale, dBm): (a) illustrates the

*Contact author: fedor.kovalev@anu.edu.au

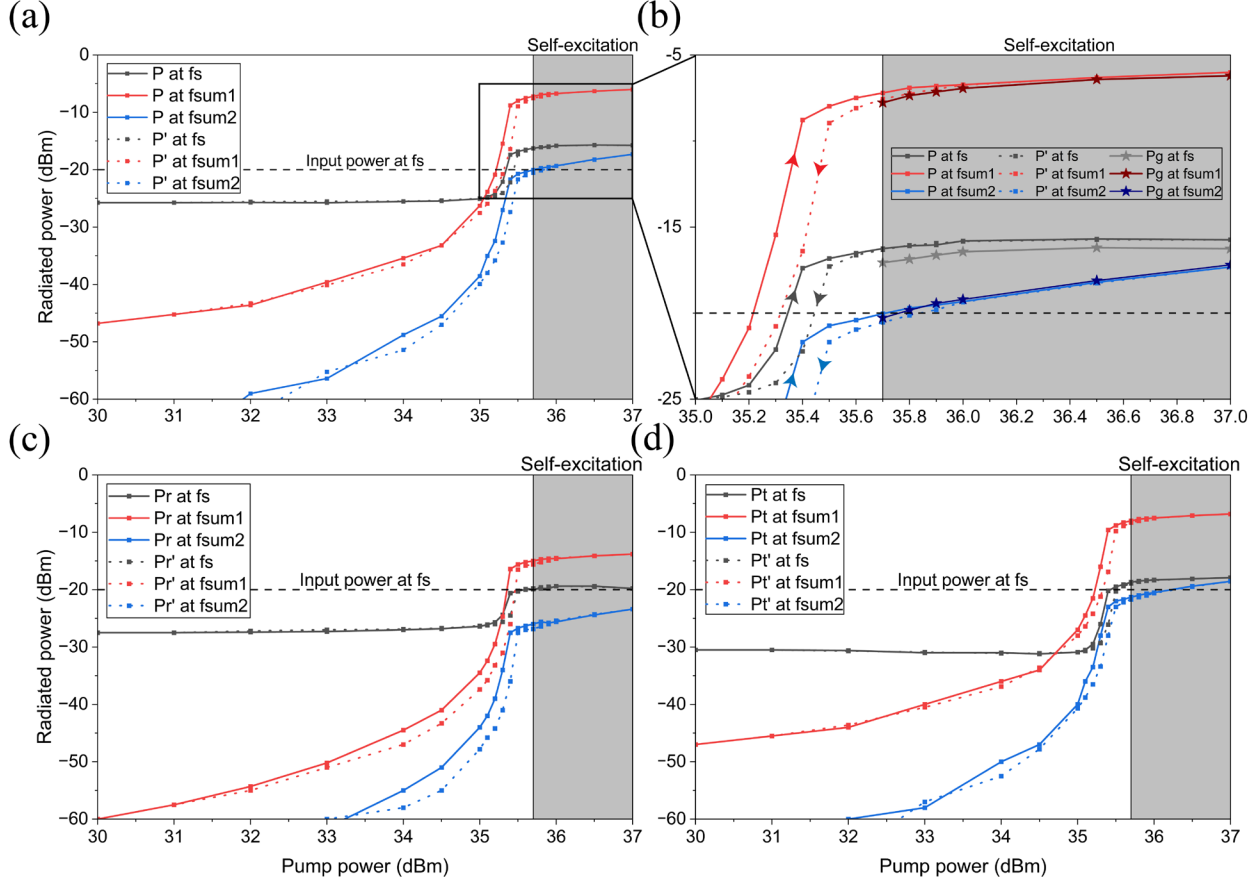


FIG 6. Dependence of the radiated power at $f_s = 316$ MHz, $f_{sum1} = 948$ MHz and $f_{sum2} = 1580$ MHz on the pump power at $f_p = 632$ MHz for $U_0 = 4$ V under phase-locking in the degenerate regime (logarithmic scale, dBm). (a) Overall radiated power; (b) same as (a) but zoomed into the region of the boundary between maximum amplification and self-generation; (c, d) power radiated in the directions of reflection and transmission, respectively, relative to the incident wave at f_s . Solid lines correspond to increasing pump power, while dotted lines correspond to decreasing pump power. The self-excitation threshold is indicated by a black vertical line at the edge of the shaded area, and the input power at f_s is shown as a horizontal dashed line.

overall response; (b) highlights the distinction between parametric amplification and generation; (c) and (d) present results in the reflection and transmission directions, respectively, relative to the propagation of the incident wave at f_s . The self-excitation threshold, at 35.7 dBm, is marked by a black vertical line at the edge of the shaded area. The input power at f_s (-20 dBm at the generator output) is indicated by a horizontal dashed line. Remarkably, the system shows hysteresis of the amplification and generation. In Figure 6, the solid lines correspond to measurements where the pump power was increased from 30 to 37 dBm, while the dotted lines show the reverse sweep from 37 to 30 dBm.

Figure 6(a) demonstrates that the overall radiated power at f_s is approximately -26 dBm at a pump level of 30 dBm. It increases slightly with pump power, reaching -25 dBm at a pump level of 35 dBm, before rising sharply up to -17 dBm. This corresponds to a

gain of ~ 3 dB relative to the input at f_s . The growth saturates around 35.5 dBm, close to the self-excitation threshold, and reaches -16 dBm at 37 dBm. A marked rectangle in Figure 6(a) highlights the section shown in Figure 6(b) for comparison with the generated power when no incident wave at f_s was present and the pump power exceeded the self-excitation threshold. Figure 6(b) demonstrates the hysteresis loop: when decreasing the pump power from 37 dBm, the dotted curve follows the solid curve almost until the self-excitation threshold, after which the loop becomes evident. The radiated powers at f_{sum1} and f_{sum2} exhibit rapid growth with pump power. At f_{sum1} , the power surpasses the input level at 35.25 dBm and approaches -8 dBm near the self-excitation threshold, corresponding to 12 dB amplification relative to the input at f_s . Notably, the radiated power at f_{sum1} is approximately 9 dB higher than that at f_s . At the self-excitation threshold, the powers at f_{sum1} and f_{sum2}

*Contact author: fedor.kovalev@anu.edu.au

reach -7 dBm and -20 dBm, respectively. Beyond threshold, the amplified up-conversion at f_{sum1} saturates, while the radiated power at f_{sum2} continues to increase slightly. The dotted lines reveal hysteresis in both sum-frequency powers, consistent with the behaviour at f_s .

Figure 6(b) highlights the hard self-excitation process, characterised by an abrupt onset of radiation (P_g) at f_s , f_{sum1} and f_{sum2} when the pump exceeds 35.7 dBm. Interestingly, Figure 6(b) shows that in the absence of an incident signal at frequency f_s , the generated power P_g above the self-excitation threshold follows a similar dependence on the pump power, with the power radiated at f_{sum1} being an order of magnitude higher than the power radiated at f_s .

Figures 6(c) and 6(d) present the directional dependence of the amplification and generation processes. In reflection, the power at f_s grows with pump power, mirroring the overall trend. In transmission, however, the power at f_s initially decreases by 1 dB before increasing rapidly above 35 dBm. The sum-frequency behaviour is similar to that discussed above. Most of the power at f_{sum1} and f_{sum2} is radiated in transmission: at 35.5 dBm, the power levels in reflection are -16 dBm and -27 dBm, compared to -9 dBm and -22 dBm in transmission.

Figure 7 shows the dependence of the overall radiated power at $f_s = 316$ MHz, $f_{sum1} = 947.9$ MHz and $f_{sum2} = 1579.9$ MHz on the pump power at $f_p = 631.9$ MHz for $U_0 = 4$ V in the non-degenerate regime (logarithmic scale, dBm).

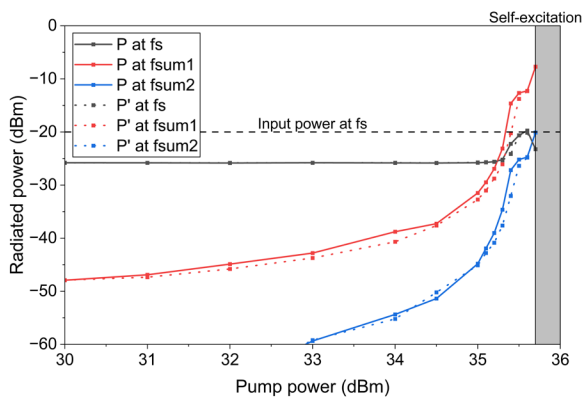


FIG 7. Overall radiated power at $f_s = 316$ MHz, $f_{sum1} = 947.9$ MHz and $f_{sum2} = 1579.9$ MHz as a function of the pump power at $f_p = 631.9$ MHz for $U_0 = 4$ V in the non-degenerate regime (logarithmic scale, dBm). Solid lines indicate increasing pump power, while dotted lines indicate decreasing pump power. The vertical line marks the self-excitation threshold, and the horizontal dashed line denotes the input power level at f_s .

The radiated power at f_s remains nearly constant (-26 dBm) until the pump power reaches 35 dBm. Beyond this point, the power grows rapidly, reaching a maximum of about -20 dBm just below the self-excitation threshold (35.7 dBm), where it drops abruptly by 3 dB. This sharp decrease indicates that part of the pump power is diverted to generate an additional component at $f_p/2 = 315.95$ MHz due to the self-excitation process. Amplification at f_s occurs primarily in transmission.

Meanwhile, the powers radiated at f_{sum1} and f_{sum2} increase rapidly with pump power up to about 35.5 dBm, after which they begin to saturate. At the instability threshold, both show an abrupt increase of approximately 4 dB. Remarkably, the overall radiated powers at f_{sum1} and f_{sum2} reach -8 dBm and -20 dBm, respectively, at the self-excitation threshold. These values are comparable to those observed in the degenerate regime. Although contributions are present in both reflection and transmission, the transmitted powers at both sum-frequencies dominate. At a pump power of 35.5 dBm, the overall radiated powers are about -21 dBm at f_s , -13 dBm at f_{sum1} , and -25 dBm at f_{sum2} . This indicates that the radiated power at f_{sum1} exceeds that at f_s by more than 7 dB in the non-degenerate regime. At this pump level, the radiated powers at f_{sum1} and f_{sum2} are -20.2 dBm and -31 dBm in reflection, and -13.5 dBm and -26.5 dBm in transmission, respectively.

Figure 8 presents the dependence of the radiated power at $f_s = 316$ MHz, f_{sum1} and f_{sum2} on the pump frequency for $U_0 = 4$ V and a pump power of 35.5 dBm in the non-degenerate regime. When the pump frequency is close to twice the signal frequency ($f_p \approx 2f_s$), the radiated power at f_s , f_{sum1} and f_{sum2} exhibits periodic temporal variations. These arise from beating between the signal and idler waves, with the beat frequency equal to their frequency difference. This beating modulates the amplitude of the radiated waves, producing fluctuations in their measured power at the beat frequency. The beating range is shown as the shaded areas in Figure 8. Away from this condition, the up-conversion efficiency decreases as the pump frequency deviates from the degenerate value. As shown in Figure 8(b), the transmitted power at f_{sum1} exceeds the input power level within the frequency range 631.65 – 632.35 MHz, corresponding to an amplified up-conversion bandwidth of less than 1 MHz. Furthermore, the experiments revealed a linear dependence of the phase of the radiated waves at f_s , f_{sum1} , and f_{sum2} on the pump phase in the non-degenerate regime, which can be used for beam steering through the appropriate spatiotemporal modulation of the metasurface parameters.

*Contact author: fedor.kovalev@anu.edu.au

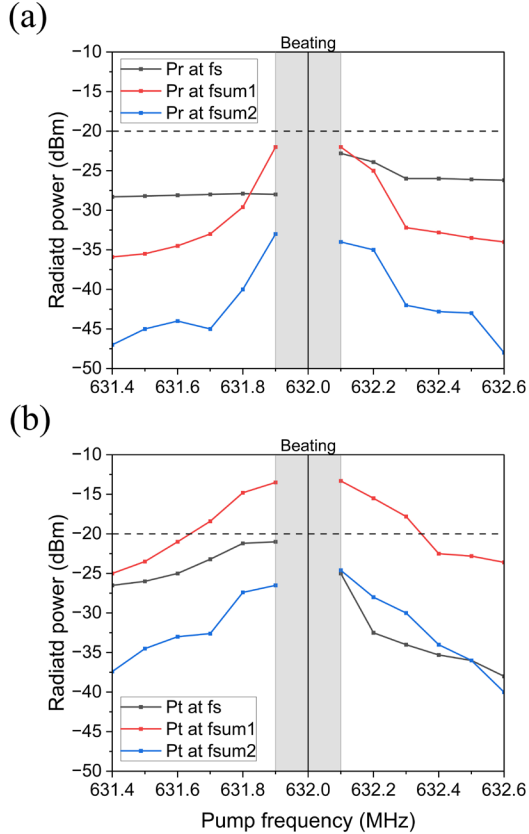


FIG 8. (a, b) Radiated power at $f_s = 316$ MHz, f_{sum1} and f_{sum2} as a function of pump frequency for $U_0 = 4$ V and a pump power of 35.5 dBm in the non-degenerate regime (logarithmic scale, dBm). The degenerate condition ($f_p = 316$ MHz) is indicated by a vertical line, while the input power at f_s (-20 dBm) is shown as a horizontal dashed line. The shaded region near the degenerate regime marks the frequency range where beating occurs in the non-degenerate regime.

IV. DISCUSSION

We experimentally demonstrate that a TVM with resonant responses near integer multiples of the signal frequency can amplify and up-convert an incident signal wave. By modulating the TVM with a pump frequency approximately twice the signal frequency we can overcome the power conversion limits imposed by the Manley–Rowe relations. This is enabled by a cascaded process in which the pump first parametrically amplifies the signal wave and subsequently up-converts it to a sum-frequency that is approximately three times higher than the incident frequency. The proposed parametric system exhibits several characteristic features, including beating phenomena in the non-degenerate regime when operating close to the degenerate frequency ratio, as

well as the requirement to maintain a precise frequency ratio and a fixed phase difference between the incident wave and the pump in the degenerate regime.

Our results provide the first demonstration of this effect in metasurfaces, and further improvements in the conversion efficiency are possible. Future work may include the design of meta-atoms that suppress radiation at the pump frequency, as well as the implementation of more efficient pump circuits. By minimising leakage of pump power into radiation at f_p , a larger fraction of the pump energy can be utilized for the conversion process. This would reduce the overall pump power required, which was a limiting factor in the experiments. Possible solutions include integrating a band-stop filter directly into the split-ring resonator structure or exploiting non-radiating modes at the pump frequency, both of which would suppress unwanted pump radiation and improve the effective energy transfer to the desired frequencies.

The integration of up-conversion and amplification within a single metasurface is highly promising for communication systems. Furthermore, as demonstrated, amplified conversion can be achieved at multiple sum-frequencies using a single signal frequency of the incident electromagnetic wave. This capability is particularly useful for designing frequency synthesizer systems in communication networks, enabling the utilization of multiple channels. Sum-frequency generation using parametric metasurfaces is also attractive for the implementation of compact terahertz radiation sources. Due to the widespread application of parametric amplification in ultrasensitive quantum computing readouts and receivers in radio astronomy and deep space communication, the proposed metasurfaces could significantly advance current technologies in this domain [29–31]. The obtained results can also be applied in the design of photonic time crystals [32,33].

V. CONCLUSION

In this work, we investigated time-varying metasurfaces and characterised their performance for parametric frequency conversion, amplification, and wave generation. We demonstrated amplified up-conversion of free-space electromagnetic waves, enabled by a cascaded parametric process that arises when the metasurface is driven by a pump frequency close to twice the signal frequency and its resonances are tuned near integer multiples of the signal frequency. Under these conditions, the power-conversion limits imposed by the Manley–Rowe relations can be surpassed. In addition, above a certain pump threshold, the metasurface enters a self-oscillation regime and operates as a generator of

*Contact author: fedor.kovalev@anu.edu.au

electromagnetic waves, predominantly at three-halves of the pump frequency. These results establish time-varying metasurfaces as a compact and efficient platform for frequency conversion, amplification, and wave generation in the microwave and terahertz regimes, with potential extension to higher frequencies using ultrafast modulation techniques and advanced material platforms.

ACKNOWLEDGMENTS

This research was supported by the Australian Research Council Centre of Excellence for Transformative Meta-Optical Systems (Project ID

CE200100010). S.M. and A.A. acknowledge funding by FCT – Fundação para a Ciência e a Tecnologia, I.P. (co-funded, when applicable, by EU funds) under the project UID/50008/2025 – Instituto de Telecomunicações, DOI:10.54499/UID/50008/2025. F.K. acknowledges support from the Robert and Helen Crompton Award.

The authors thank David Powell, Andrea Alù, Akshaj Arora, Puneet Garg, Zachary Fritts and Vitali Kozlov for useful discussions, as well as Michael Blacksell, Steve Marshall, Matthew Holding, José Carlos Pedro, Luís Cótimos Nunes and António Correia for assistance and guidance in preparing the experiment.

- [1] A. M. Shaltout, V. M. Shalaev, and M. L. Brongersma, Spatiotemporal light control with active metasurfaces, *Science* **364**, eaat3100 (2019).
- [2] C. Caloz and Z.-L. Deck-Léger, Spacetime Metamaterials—Part I: General Concepts, *IEEE Trans. Antennas Propagat.* **68**, 1569 (2020).
- [3] F. R. Morgenthaler, Velocity Modulation of Electromagnetic Waves, *IEEE Trans. Microwave Theory Techn.* **6**, 167 (1958).
- [4] E. S. Casseddy and A. A. Oliner, Dispersion relations in time-space periodic media: Part I—Stable interactions, *Proc. IEEE* **51**, 1342 (1963).
- [5] E. S. Casseddy, Dispersion relations in time-space periodic media part II—Unstable interactions, *Proc. IEEE* **55**, 1154 (1967).
- [6] E. Galiffi, R. Tirole, S. Yin, H. Li, S. Vezzoli, P. A. Huidobro, M. G. Silveirinha, R. Sapienza, A. Alù, and J. B. Pendry, Photonics of time-varying media, *Adv. Photon.* **4**, (2022).
- [7] S. Taravati and G. V. Eleftheriades, Microwave Space-Time-Modulated Metasurfaces, *ACS Photonics* **9**, 305 (2022).
- [8] N. Engheta, Four-dimensional optics using time-varying metamaterials, *Science* **379**, 1190 (2023).
- [9] Z. Hayran and F. Monticone, Using Time-Varying Systems to Challenge Fundamental Limitations in Electromagnetics: Overview and summary of applications, *IEEE Antennas Propag. Mag.* **65**, 29 (2023).
- [10] A. Shaltout, A. Kildishev, and V. Shalaev, Time-varying metasurfaces and Lorentz non-reciprocity, *Opt. Mater. Express* **5**, 2459 (2015).
- [11] D. L. Sounas and A. Alù, Non-reciprocal photonics based on time modulation, *Nature Photon* **11**, 774 (2017).
- [12] C. Caloz, A. Alù, S. Tretyakov, D. Sounas, K. Achouri, and Z.-L. Deck-Léger, Electromagnetic Nonreciprocity, *Phys. Rev. Applied* **10**, 047001 (2018).
- [13] T. Liu, J.-Y. Ou, K. F. MacDonald, and N. I. Zheludev, Photonic metamaterial analogue of a continuous time crystal, *Nat. Phys.* **19**, 986 (2023).
- [14] M. M. Asgari, P. Garg, X. Wang, M. S. Mirmoosa, C. Rockstuhl, and V. Asadchy, Theory and applications of photonic time crystals: a tutorial, *Adv. Opt. Photon.* **16**, 958 (2024).
- [15] R. Tirole, S. Vezzoli, E. Galiffi, I. Robertson, D. Maurice, B. Tilmann, S. A. Maier, J. B. Pendry, and R. Sapienza, Double-slit time diffraction at optical frequencies, *Nat. Phys.* **19**, 999 (2023).
- [16] S. Taravati and A. A. Kishk, Space-Time Modulation: Principles and Applications, *IEEE Microwave* **21**, 30 (2020).
- [17] J. T. Mendonça and P. K. Shukla, Time Refraction and Time Reflection: Two Basic Concepts, *Phys. Scr.* **65**, 160 (2002).
- [18] H. Moussa, G. Xu, S. Yin, E. Galiffi, Y. Ra'di, and A. Alù, Observation of temporal reflection and broadband frequency translation at photonic time interfaces, *Nat. Phys.* **19**, 863 (2023).
- [19] E. Lustig et al., Time-refraction optics with single cycle modulation, *Nanophotonics* **12**, 2221 (2023).
- [20] P. Hannaford and K. Sacha, Reflection and refraction at a time boundary, *Nat. Photon.* **18**, 7 (2024).
- [21] E. Galiffi, P. A. Huidobro, and J. B. Pendry, Broadband Nonreciprocal Amplification in Luminal Metamaterials, *PHYSICAL REVIEW LETTERS* **6** (2019).
- [22] J. B. Pendry, E. Galiffi, and P. A. Huidobro, Gain in time-dependent media—a new

*Contact author: fedor.kovalev@anu.edu.au

mechanism, *J. Opt. Soc. Am. B* **38**, 3360 (2021).

[23] M. Lyubarov, Y. Lumer, A. Dikopoltsev, E. Lustig, Y. Sharabi, and M. Segev, Amplified emission and lasing in photonic time crystals, *Science* **377**, 425 (2022).

[24] X. Wang, M. S. Mirmoosa, V. S. Asadchy, C. Rockstuhl, S. Fan, and S. A. Tretyakov, Metasurface-based realization of photonic time crystals, *Sci. Adv.* **9**, eadg7541 (2023).

[25] F. V. Kovalev and I. V. Shadrivov, Parametric metasurfaces for electromagnetic wave amplification, *Opt. Mater. Express* **14**, 494 (2024).

[26] F. Deng, F. Zhu, X. Zhou, Y. Chan, J. Wu, C. Zhang, B. Jin, J. Li, K. Fan, and J. Zhang, Frequency-Selective Terahertz Wave Amplification by a Time Boundary in Huygens' Metasurface, *Advanced Optical Materials* **13**, 2402052 (2025).

[27] J. Manley and H. Rowe, Some General Properties of Nonlinear Elements-Part I. General Energy Relations, *Proc. IRE* **44**, 904 (1956).

[28] F. Kovalev and I. Shadrivov, Parametric metasurfaces for amplified upconversion of electromagnetic waves, *Applied Physics Letters* **126**, 261702 (2025).

[29] J. Aumentado, Superconducting Parametric Amplifiers: The State of the Art in Josephson Parametric Amplifiers, *IEEE Microwave* **21**, 45 (2020).

[30] L. Fasolo, A. Greco, and E. Enrico, *Superconducting Josephson-Based Metamaterials for Quantum-Limited Parametric Amplification: A Review*, in *Advances in Condensed-Matter and Materials Physics - Rudimentary Research to Topical Technology*, edited by J. Thirumalai and S. Ivanovich Pokutnyi (IntechOpen, 2020).

[31] D. J. Parker, M. Savytskyi, W. Vine, A. Laucht, T. Duty, A. Morello, A. L. Grimsmo, and J. J. Pla, Degenerate Parametric Amplification via Three-Wave Mixing Using Kinetic Inductance, *Phys. Rev. Applied* **17**, 034064 (2022).

[32] S. Saha, O. Segal, C. Fruhling, E. Lustig, M. Segev, A. Boltasseva, and V. M. Shalaev, Photonic time crystals: a materials perspective [Invited], *Opt. Express* **31**, 8267 (2023).

[33] A. Boltasseva, V. M. Shalaev, and M. Segev, Photonic time crystals: from fundamental insights to novel applications: opinion, *Opt. Mater. Express* **14**, 592 (2024).

*Contact author: fedor.kovalev@anu.edu.au

Supplementary material for the paper “Amplified up-conversion of electromagnetic waves using time-varying metasurfaces”

Fedor Kovalev,^{1,*} Stanislav Maslovski,² Abdelghafour Abraray,² and Ilya Shadrivov¹

¹ ARC Centre of Excellence for Transformative Meta-Optical Systems (TMOS), Research School of Physics, The Australian National University, Canberra ACT 2601, Australia

² Instituto de Telecomunicações and Department of Electronics, Telecommunications and Informatics, University of Aveiro, Aveiro, 3810 – 193, Portugal

Figure S1 illustrates the schematic of the varactor diode MGV100-20 SPICE model, along with the pump and biasing circuit attached to the meta-atom in CST Studio. The SPICE model incorporates the parasitic capacitance and inductance of the 0805-02 package and the resistance of the varactor diode: $R_s = 0.3$ Ohm, $C_p = 0.06$ pF, $L_p = 0.4$ nH. The varactor diode is modulated through a filtering circuit consisting of a passband LC filter at f_p ($C_{ac} = 0.1$ pF and $L_{ac} = 370$ nH, with the parasitic capacitance $C_{pac} = 0.0685$ pF) connected in series with an ac source of 50Ω impedance, and a choke connected to a dc source ($L_{dc} = 500$ nH with the parasitic capacitance $C_{pdc} = 0.063$ pF). The passband filter at f_p is designed for protecting the microwave generator from the dc and ac currents at f_s , f_{sum1} and f_{sum2} . The circuits incorporate the parasitic capacitances of the inductors, which significantly affect the characteristics of the time-varying meta-atoms due to the small capacitance of the varactor diodes.

Figure S2 presents the meta-atom design consisting of two perpendicularly arranged printed circuit boards (PCB) based on the Rogers RO4350B substrates of thickness 0.51 mm, with dielectric permittivity $\varepsilon_r = 3.66$ and loss tangent $\tan\delta = 0.0037$ used in CST Studio modeling. The resonator parameters are $R_1 = 21$ mm, $R_2 = 12$ mm, $w = 1.116$ mm, $g_1 = 1$ mm, $g_2 = 0.6$ mm, $d = 0.543$ mm. The microstrip dimensions are $w = 1.116$ mm, $g_2 = 0.6$ mm, $g_3 = 0.45$ mm, $w_{dc} = 0.64$ mm, $l_{dc} = 19.434$ mm, $a_{dc} = 0.78$ mm, $l_{ac} = 10.456$ mm, $l_{m1} = 23.616$ mm, $l_{m2} = 6.508$ mm, $l_{m3} = 2$ mm. The pad connecting the resonators to ground has the following size: $w = 1.116$ mm and $w_p = 1.081$ mm, with via diameter of 0.6 mm. The ac microstrip width (w) was selected to realise a $50\text{-}\Omega$ transmission line at f_p . Copper thickness is 35 μm throughout.

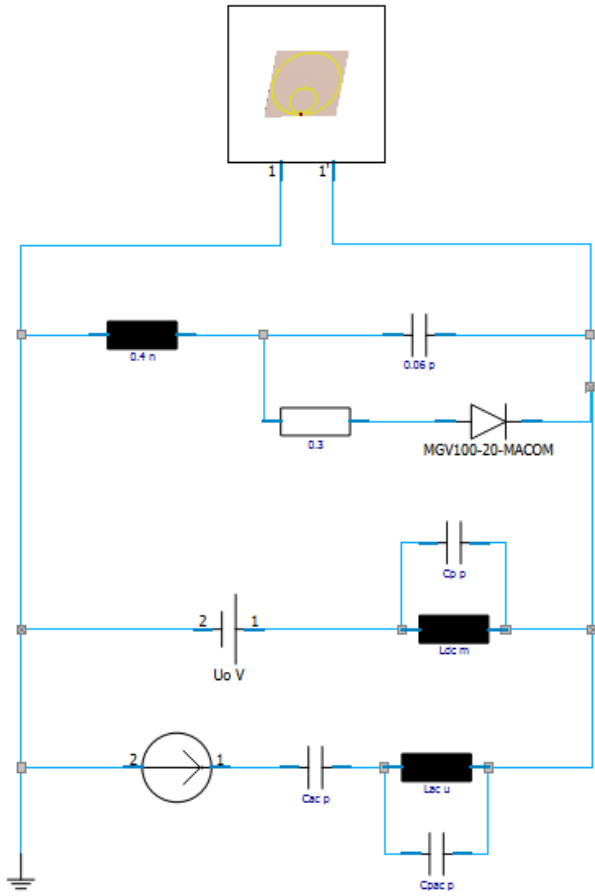


FIG S1. Schematic of the varactor diode MGV100-20 SPICE model, along with the pump and biasing circuit attached to the meta-atom in CST Studio.

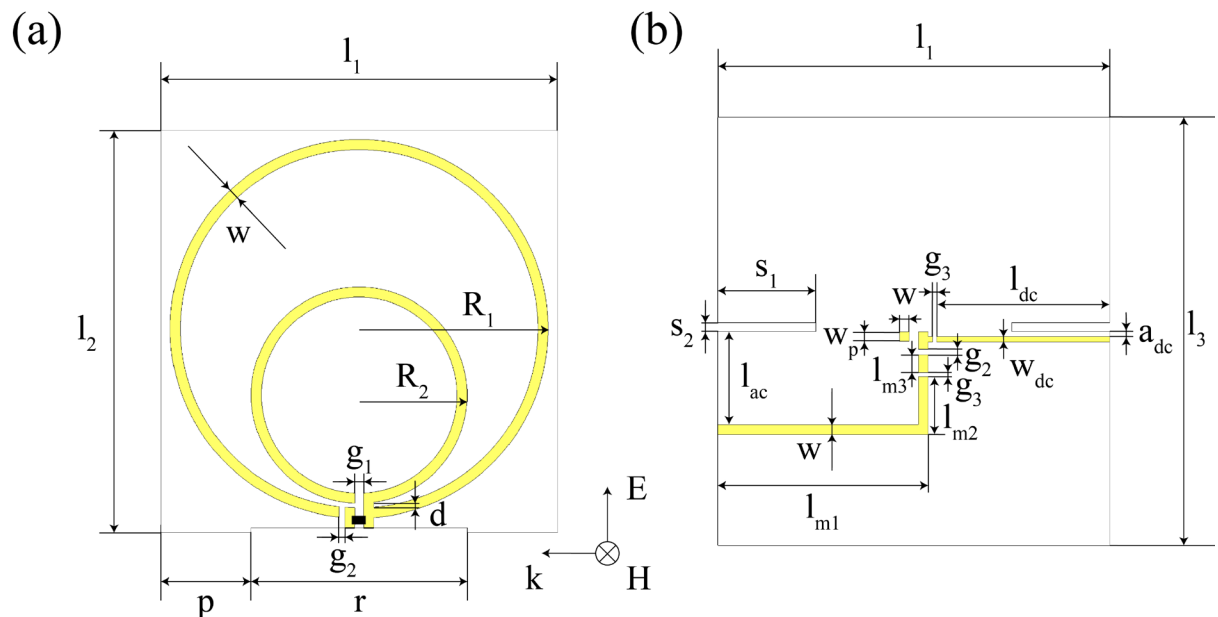


FIG S2. Meta-atom design: (a) vertical circuit board with two connected split-ring resonators and an embedded varactor diode (black square); (b) horizontal circuit board with the microstrips.

The circuit boards have dimensions $l_1 = 44$ mm, $l_2 = 44.51$ mm, $l_3 = 48$ mm. The horizontal board includes two slots ($s_1 = 11$ mm, $s_2 = 1.123$ mm) for inserting two protrusions of the vertical board ($p = 10$ mm) spaced by $r = 24$ mm. After soldering the lumped elements, the two circuit boards were glued together, and finally the pads of the horizontal board were soldered to the split-ring resonators. In our experiments, the ac microstrip line was connected to a coaxial cable using a standard coaxial connector, and the dc microstrip line was connected to a dc source using a regular dc cable.

In CST Studio simulations, we use discrete ports in the gaps and ends of the microstrip lines to simulate the corresponding circuit elements and sources. We conduct full-wave numerical simulations of the periodic structure using the finite-element method and transfer the 3D modeling results to the Schematic simulator in CST Studio to model the nonlinear lumped element circuit, which includes the varactor diode and the biasing network. S-parameters task was used for obtaining the reflection characteristics of the metasurface.

For obtaining the amplification and frequency conversion characteristics, we utilize the Spectral Lines task within the Schematic module of CST Studio to simulate the nonlinear circuit in the frequency domain. This approach leverages Harmonic Balance (HB) analysis, allowing us to investigate the interaction between the pump and signal within the designed circuit. The method accounts for frequency mixing up to a defined harmonic limit. To accurately capture the mixing effects, we consider 20 harmonics for the signal source and 10 harmonics for the pump source. In this study, the highest-order pump and signal harmonics considered in the simulations occur at nearly the same frequencies, ensuring that the harmonic balance analysis accurately captures their interaction.

Figures S3(a-d) demonstrate that the metasurface radiates more power at the sum frequencies in transmission than in reflection. While the reflected power at f_s increases monotonically with pump amplitude, the transmitted power at f_s initially decreases until $U_p \approx 8$ V, after which it rises sharply with further increases. This behaviour is consistent with previously discussed parametric amplification phenomena in Ref. 25.

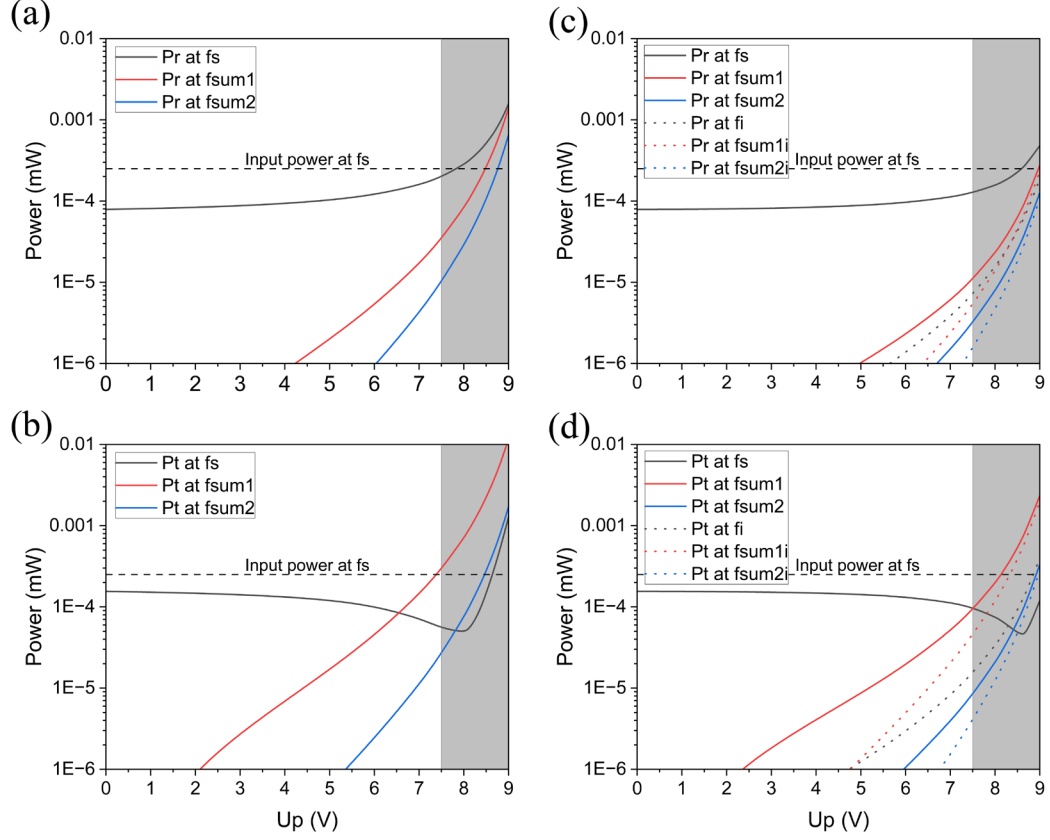


FIG S3. Radiated power versus pump amplitude for $U_0 = 10$ V (logarithmic scale). (a, b) Degenerate regime under phase-locking conditions with $f_s = 320$ MHz, $f_p = 640$ MHz, $f_{sum1} = 960$ MHz and $f_{sum2} = 1600$ MHz: (a) reflection and (b) transmission relative to the incident wave at f_s . (c, d) Non-degenerate regime with $f_s = 320$ MHz, $f_i = 319.9$ MHz, $f_p = 639.9$ MHz, $f_{sum1} = 959.9$ MHz, $f_{sum1i} = 959.8$ MHz, $f_{sum2} = 1599.9$ MHz and $f_{sum2i} = 1599.8$ MHz: (c) reflection and (d) transmission. The input power level at f_s is indicated by the horizontal dashed line. The shaded region corresponds to $U_p > 7.5$ V, where the varactor model becomes inaccurate.

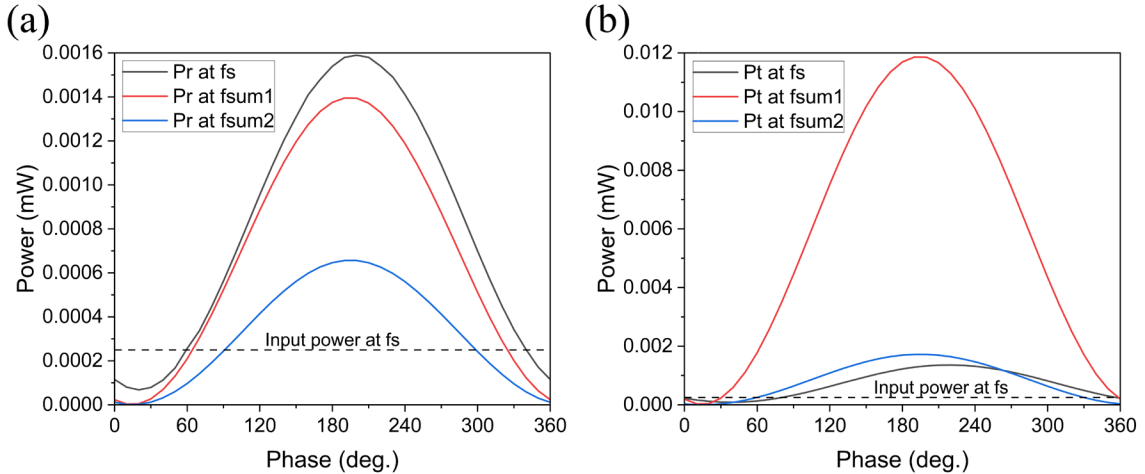


FIG S4. Radiated power at $f_s = 320$ MHz, $f_{sum1} = 960$ MHz and $f_{sum2} = 1600$ MHz versus pump phase at $f_p = 640$ MHz for $U_0 = 10$ V and $U_p = 9$ V in the degenerate regime: (a) reflection and (b) transmission relative to the incident wave at f_s .

Figure S4 shows the dependence of the radiated power at $f_s = 320$ MHz, $f_{sum1} = 960$ MHz and $f_{sum2} = 1600$ MHz on the pump phase at $f_p = 640$ MHz for $U_0 = 10$ V and $U_p = 9$ V in the degenerate regime, in both reflection and transmission directions relative to the incident wave at f_s . The results in Figures 3(a) and S3(a, b) correspond to a pump phase of 190° , which yields the maximum radiated power at f_{sum1} . Figure S4 demonstrates that the radiated power at f_s , f_{sum1} and f_{sum2} follows a nearly sinusoidal dependence on the pump phase in the degenerate regime.

Figure S5 presents a schematic of the TEM cell used in the experiments. It consists of two parts: the ground and the stripline. The ground plane has dimensions of 684 mm \times 305 mm. The stripline comprises three segments: a central part (228 mm \times 252 mm) and two side parts (252 mm \times 255.14 mm \times 23 mm). The distance between the central stripline and the ground is 45 mm, while the shortest facets of the side parts are separated from the ground by 5 mm. The dimensions of the ground and the stripline were selected in a way to maintain approximately uniform characteristic impedance along the whole TEM cell.

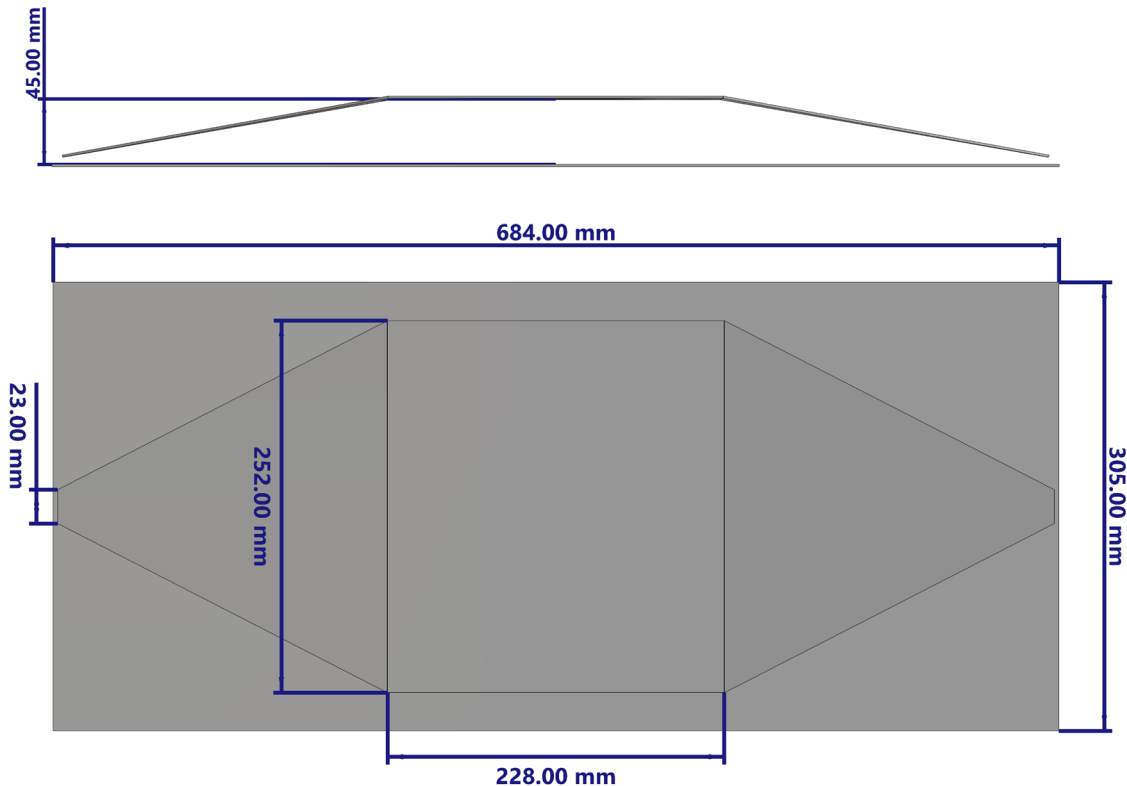


FIG S5. TEM cell and its dimensions.

Figure S6 illustrates the electric and magnetic fields in a plane perpendicular to the stripline and the ground plane when the TEM cell is excited at one port (shown as red cones) at 320 MHz. The fields are predominantly confined between the stripline and the ground plane, with the electric field oriented normal to these conductors and the magnetic field parallel to them. The stripline and the ground plane impose electric-wall boundary conditions, while the open lateral boundaries provide an approximate magnetic-wall symmetry. These symmetries are equivalent to the use of electric and magnetic mirror planes commonly employed to simulate infinite periodic structures. Consequently, when the meta-atom array is appropriately positioned with respect to these symmetry boundaries, the excitation conditions inside the TEM cell emulate those of an infinite periodic metasurface under plane-wave illumination.

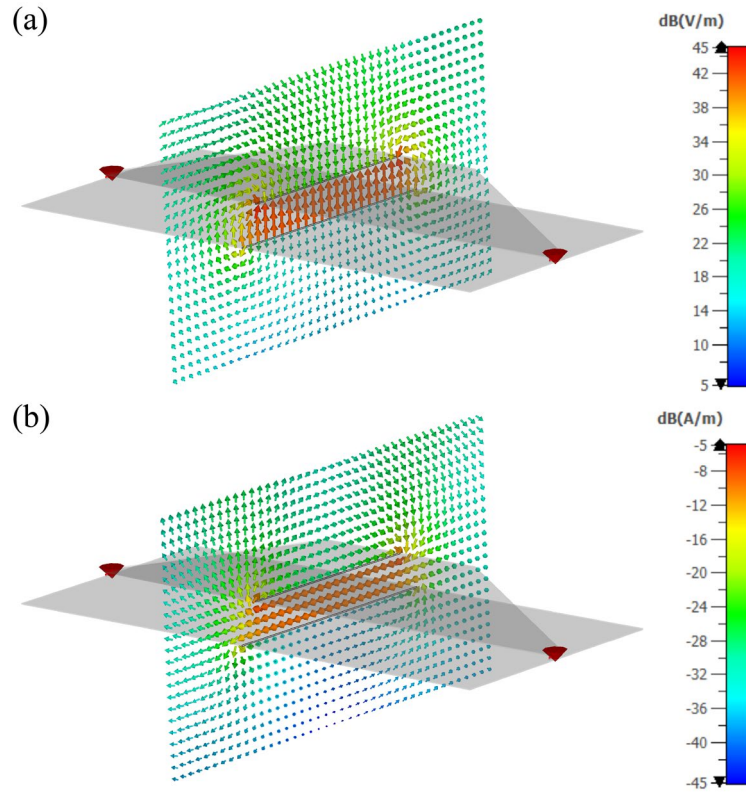


FIG S6. (a, b) Electric and magnetic field in the plane perpendicular to the TEM cell stripline and ground when excited at 320 MHz from one of its ports, shown as red cones.

Figure S7 shows the modeled and measured S-parameters of the TEM cell. The measurements were performed using a Keysight PNA-X N5242A vector network analyzer. The results confirm the expected performance: although the measured reflection (S_{22}) is slightly higher at high frequencies and the transmission (S_{21}) at 960 MHz is -4 dB compared to -2 dB in simulations, the reflection remains below -10 dB for frequencies up to 1350 MHz, which is sufficient to accurately measure the up-conversion characteristics at f_{sum1} .

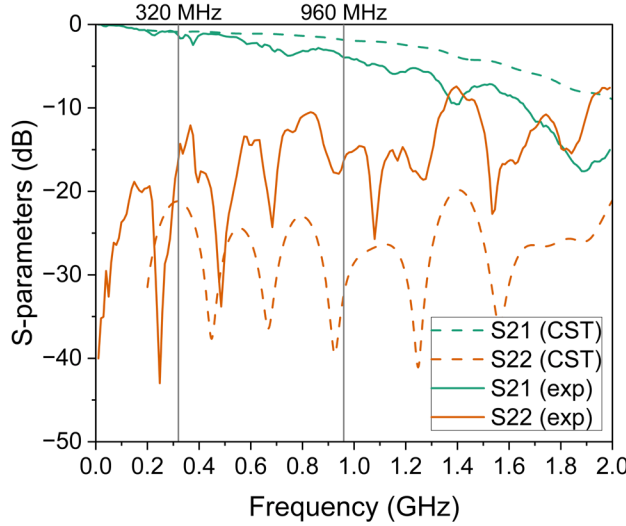


FIG S7. The simulated (dashed) and measured (solid) S-parameters of the TEM cell. The vertical lines at 320 and 960 MHz highlight the TEM cell performance around f_s and f_{sum1} .

The developed TEM cell model was further used to obtain the scattering characteristics of seven meta-atoms excited at f_s from one of its ports, as illustrated in Figure S8. For the numerical implementation, lumped ports loaded with equivalent inductance, capacitance, and resistance were employed to represent the meta-atom's lumped elements. The first lumped port in the SRR gap included $L_{dc} = 500$ nH and C_{sum} (the sum of the varactor diode capacitance and parasitic capacitances; we used two values: $C_{max} = 1.2$ pF corresponding to $U_0 = 2$ V, $C_{min} = 0.4$ pF corresponding to $U_0 = 20$ V) in parallel. The second lumped port connected to the ac microstrip line incorporated $C_{ac} = 0.1$ pF, $L_{ac} = 370$ nH, and $R_g = 50 \Omega$ in series. The number of meta-atoms and their spacing were selected such that, in combination with the electric- and magnetic-wall symmetries of the TEM cell, the array emulates the response of an infinite periodic metasurface, ensuring in-phase excitation of all SRRs at f_s and preserving the required tunability of the resonant responses.

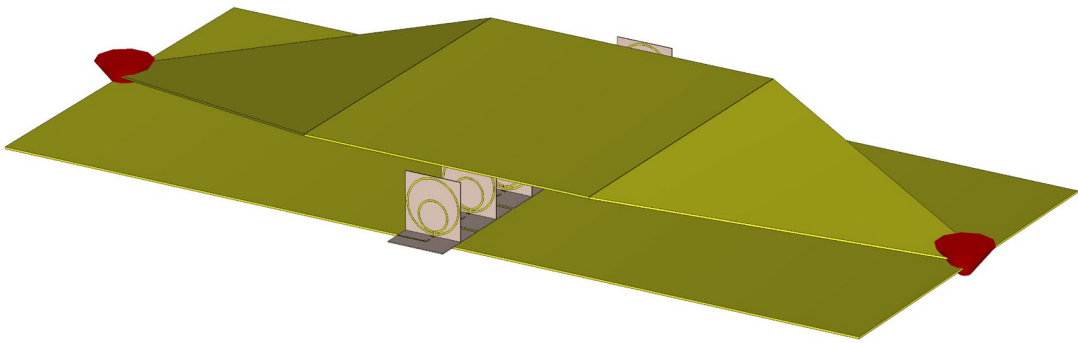


FIG S8. Model of the TEM cell with 7 meta-atoms placed on the ground plane.

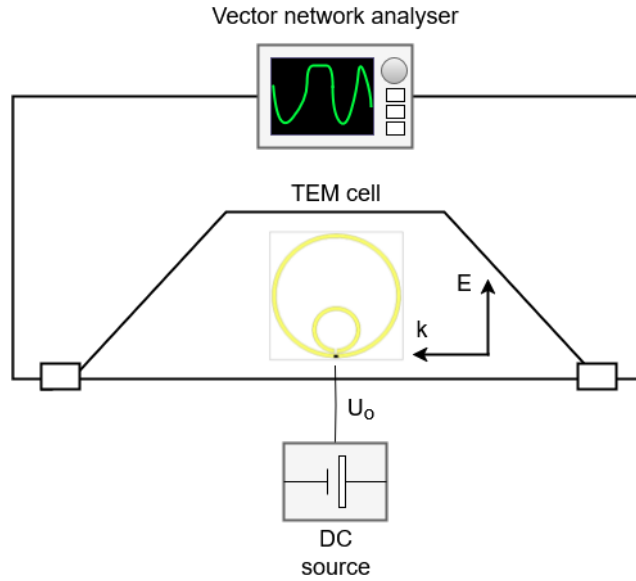


FIG S9. Diagram showing the S-parameters measurement scheme.

The S-parameters of the meta-atoms were measured using a Keysight PNA-X N5242A, as shown in Figure S9. Connections were made via vertical coaxial connectors mounted on the ground plane of the TEM cell, with their central conductors soldered to the stripline. For these measurements, the coaxial pump connectors were terminated with 50Ω loads. Figure S9 also indicates the electric field direction and the wavevector of the excited TEM mode.

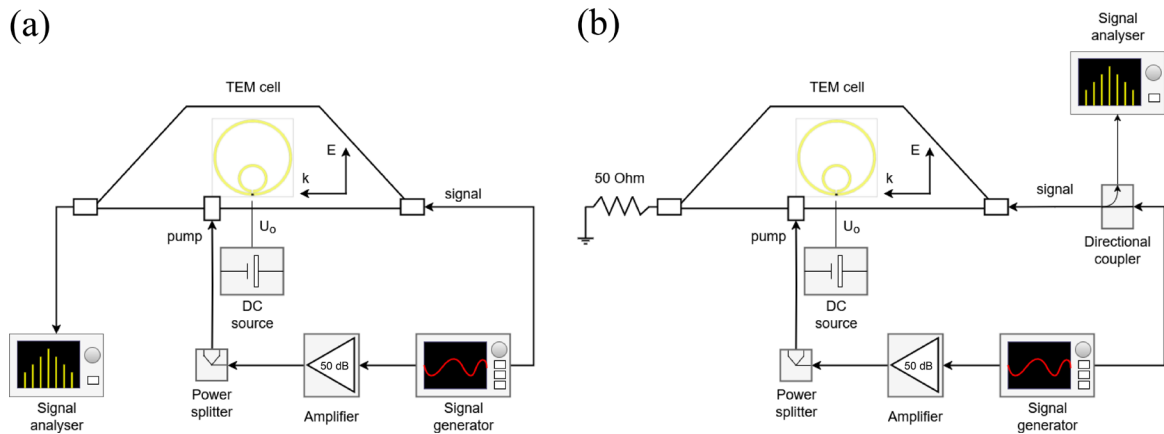


FIG S10. (a, b) Microwave experimental setup for measurements of up-conversion, amplification and generation characteristics of the time-varying meta-atoms in transmission and reflection.

Figure S10(a,b) presents the experimental setup used to measure up-conversion, amplification and generation of electromagnetic waves with the time-varying meta-atoms in the TEM cell, in transmission and reflection configurations, respectively. The system comprised a Rohde & Schwarz FSQ8 signal analyzer, a Rohde & Schwarz SMW200A two-port signal generator, a

ZHL-30W-252-S+ power amplifier (providing 50 dB gain), a ZBSC-8-82+ power splitter, and an MX100QP dc source. A directional coupler (FDC-20-5-S+) was employed to measure the power of the radiated waves at the same port used to excite the incident wave, as it is shown in Figure S10(b). To enable this configuration, the opposite port was terminated with a $50\ \Omega$ load to absorb propagating waves. Since only one port could be monitored at a time, the measurements in reflection and transmission had to be performed separately.

Additionally, we analyze the phase dependence of the radiated power in the degenerate regime. Figure S11 shows the radiated power at $f_s = 313$ MHz, $f_{sum1} = 939$ MHz, and $f_{sum2} = 1565$ MHz in the directions of reflection and transmission as a function of the pump phase for $U_0 = 3$ V and a pump power of 32.7 dBm at $f_p = 626$ MHz. While the radiated power in reflection remains below the incident wave power (shown as a horizontal dashed line), the radiated power at f_{sum1} in transmission can exceed this level when the pump phase is properly aligned with the signal phase. In addition, the minima and maxima of the radiated waves at f_s are shifted differently relative to those at the sum-frequencies in both reflection and transmission. Although the experimental setup does not allow a direct comparison of reflection and transmission phase dependence (the directional coupler introduces an additional phase shift in reflection measurements), the results nevertheless confirm the dependence of the radiated waves on the pump phase in the degenerate regime and show good agreement with numerical modeling (see Figure S4).

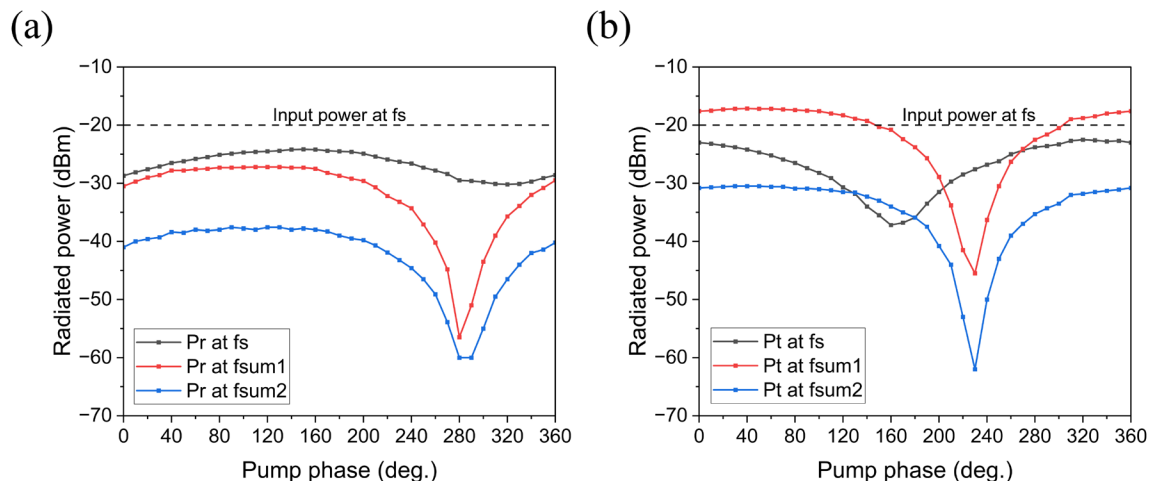


FIG S11. (a, b) Dependence of the radiated power at $f_s = 313$ MHz, $f_{sum1} = 939$ MHz, and $f_{sum2} = 1565$ MHz on the pump phase for $U_0 = 3$ V and a pump power of 32.7 dBm at $f_p = 626$ MHz in the degenerate regime. The horizontal dashed line indicates the input power level at f_s .